Materials Advances

ROYAL SOCIETY OF CHEMISTRY

PAPER

View Article Online
View Journal | View Issue

Cite this: *Mater. Adv.*, 2024, 5, 5118

Engineering of efficient functionalization in a zirconium-hydroxyl-based metal–organic framework for an ultra-high adsorption of Pb^{2+} ions from an aqueous medium: an elucidated uptake mechanism†

Hang M. N. Pham, Anh V. N. Phan, Anh N. T. Phan, Vi P. Nguyen, Khang M. V. Nguyen, Hung N. Nguyen, Thai M. Nguyen and My V. Nguyen *

Metal–organic framework (MOF) adsorbents have been proven to possess an effective Pb^{2+} uptake property in recent years. However, their abilities are inadequate for industrial and real-life situations due to their ineffective adsorption capacity and lack of modified engineering. To overcome these disadvantages, a new hydroxyl-functionalized Zr-based-MOF, denoted as HCMUE-2, was successfully synthesized through the solvothermal method. The Pb^{2+} adsorption onto HCMUE-2 was completely observed under optimal conditions, including solution pH, MOF content, adsorption isotherms, and kinetics. Consequently, the maximum Pb^{2+} adsorption capacity over the OH-modified HCMUE-2 is 1115.9 mg g^{-1} at a pH value of 5.5, which is one of the highest values compared with the previously reported MOFs. Additionally, the obtained data for Pb^{2+} uptake is fitted with the Langmuir isotherm and pseudo-second-order models, indicating that the removal of Pb^{2+} onto HCMUE-2 is a chemical adsorption process. Notably, HCMUE-2 can maintain the adsorption efficiency of Pb^{2+} by about 93% after seven consecutive cycles. Furthermore, the Pb^{2+} uptake mechanism is elucidated by systematically incorporated analyses. Accordingly, Fourier transform infrared and Raman spectroscopies, thermogravimetric analysis combined with differential scanning calorimetry, energy-dispersive X-ray, and X-ray photoelectron spectroscopy of Pb⊂HCMUE-2 show that the chemical bonds are formed *via* the electrostatic interaction and electron sharing between hydroxyl moieties within the MOF architecture and the Pb^{2+} species. It is noteworthy that HCMUE-2 is a potential material for removing Pb^{2+} from wastewater.

Received 8th April 2024,
Accepted 26th April 2024

DOI: 10.1039/d4ma00369a

rsc.li/materials-advances

1. Introduction

With the rapid growth of various industries, a huge amount of toxic pollutants are purged to water sources without treatment, resulting in severe water surrounding contamination. Hence, wastewater containing heavy metal ions such as mercury, copper, chromium, and lead with high content has received much attention in many studies to minimize their harmful effects on the environment and human health.[1,2] Among these, lead has been classified as a highly poisonous ion with a long biological half-life of up to 30 years in aquatic media. Particularly, the prompt developments of lead-acid batteries, metal mining and smelting, aircraft transportation, and the fertilizer industry have caused secondary lead release into ecosystems.[3–6] The exposure and presence of lead in organisms have posed irreversible damage to the human body, including kidney and liver failure, accumulation, rickets, anemia, and cancer.[2,5] The maximum allowable amount of Pb^{2+} in freshwater is 0.01–0.015 ppm according to the Environmental Protection Agency (EPA) and World Health Organization (WHO). Various methods such as precipitation,[7,8] ion exchange,[9,10] ultrafiltration,[11,12] and adsorption[13–15] have been employed for lead-contaminated water treatment. It is noteworthy that the procedures, including precipitation, ion exchange, and ultrafiltration, have several advantages in terms of user-friendliness and economic efficiency. However, there are disadvantages to using these adsorbents, such as low selectivity, poor flexibility, and slow rate. Besides these methods, adsorption has been widely used owing to its high efficiency, low cost, rapid treatment,

Faculty of Chemistry, Ho Chi Minh City University of Education, Ho Chi Minh City, 700000, Vietnam. E-mail: mynv@hcmue.edu.vn

† Electronic supplementary information (ESI) available. See DOI: https://doi.org/10.1039/d4ma00369a

high selectivity, and adaptability.[16–18] Many traditional materials such as chitosan, graphite oxide, zeolite, and active carbon are used to eliminate heavy metal ions from aqueous media.[19–22] Nevertheless, these materials possess several drawbacks, including prolonged adsorption rate, poor functionalization, and low uptake capacity, because they lack strong attractions between the active sites of absorbents and adsorbates. Therefore, it is urgent to seek novel alternative absorbents to effectively remove the Pb^{2+} ions from wastewater under practical conditions. Recently, metal–organic frameworks (MOFs) have attracted numerous studies in the efficient purging of heavy metal ions from wastewater due to their extraordinary properties, such as high specific surface area, versatile structure with high crystallinity, and easy post-synthetic modification.[23,24] To date, MOFs have been reported with potential applications in many fields, including catalysis,[25–28] separation,[29,30] sensor,[31,32] energy storage,[33,34] and adsorption.[35–38] Noteworthily, the MOF architecture can be adjusted by functional groups to enhance the interactions between the adsorption sites and guest moieties, driving new promising approaches with respect to adsorption. In particular, zirconium-based MOFs are well known as highly water-stable materials due to their rigid backbone and stable metal–carboxylate bonds, opening excellent applications in real-life situations. In fact, the most common MOFs are found to have low capacity and efficiency for Pb^{2+} uptake. This limitation can be attributed to the lack of efficient electrostatic attraction of active sites with positively charged species of the Pb^{2+} ions. Thus, engineering MOFs with specific modified groups containing unpaired electrons, such as amino, sulfonic, thiol, and hydroxyl, to improve electrostatic interactions with Pb^{2+} is a potential pathway for overcoming the stated disadvantages. Accordingly, amino-functionalized Zr-MOF was fabricated by Yin *et al.*, indicating a Pb^{2+} uptake of 135.0 mg g^{-1}.[39] In our previous work, we prepared a Zr-MOF containing sulfonic moieties, termed VNU-23, exhibiting a high Pb^{2+} adsorption ability of 617.3 mg g^{-1} at pH = 5.5.[40] It is noteworthy that hydroxyl groups (–OH) have lone pair electrons, which are known as Lewis bases that can support the generation of strong coordination bond with the Pb^{2+} ions. Moreover, the presence of –OH groups within the MOF architecture could obtain many advantages to meet the criteria for boosting the fast adsorption kinetics and greater uptake capacity of Pb^{2+}: (i) providing chelation and hydrogen-bonding sites inside the aromatic and nonpolar linkers; (ii) forming three-dimensional flexible crystal structure and electron-donating ability of specific atoms of functional groups with guest species.[41] This engineering strategy is sucessfully applied to UiO-66-OH and UiO-66-$(OH)_2$, which indicate effective adsorption capacities for Cr(VI) and Co(II) ions of 39.0 mg g^{-1} and 133.3 mg g^{-1}, respectively.[42,43] Inspired by these aspects, we expect that if the combination of OH-modified linkers and zirconium clusters to create a new MOF class is successfully performed, it enhances the Pb^{2+} removal level from an aqueous medium *via* the available interactions of hydroxyl groups inside MOF with the Pb^{2+} ion. This is a new direction for coping with the mentioned limitations in terms of the uptake capacity and adsorption rate of Pb^{2+} in the previously reported literature.

In this contribution, a new hydroxyl-functionalized Zr-based-MOF, denoted as HCMUE-2, was successfully synthesized *via* a solvothermal procedure with an ultra-high Pb^{2+} adsorption capacity of 1115.9 mg g^{-1} at pH = 5.5. Notably, complete structural characterizations and the Pb^{2+} adsorption mechanism onto HCMUE-2 were interpreted through the adsorption models combined with the analytical procedures. Furthermore, the cost-effectiveness of the synthesized material is relatively low and acceptable for practical applications. These findings indicate that HCMUE-2 is a potential candidate for efficiently eliminating Pb^{2+} ions from wastewater.

2. Experimental section

Starting reagents and procedures

All chemicals were purchased from commercial suppliers and directly used for further investigation. Zirconium(IV) oxychloride octahydrate ($ZrOCl_2{\cdot}8H_2O$, 99%), 2,6-naphthalene dicarboxylic acid (H_2NDC, 98%), oleum (SO_3 in concentrated H_2SO_4, 20%), *N*,*N*-dimethylformamide (DMF, 98%), hydrochloric acid (HCl, 37%), methanol (MeOH, 99%), and acetonitrile (99%) were supplied from local vendors. The linker of 4,8-disulfonaphthalene-2,6-dicarboxylic acid (H_4SNDC) was prepared through the sulfonic-modified process described in a previous work.[40]

Powder X-ray diffraction (PXRD) data were recorded on a Ni-filtered Cu Kα source (λ = 1.54718 Å) using a diffractometer (D8 Advance, Bruker). The 2θ range was 3–50° with a step size of 0.02° and a fixed counting time of 0.3 s per step. Fourier transform infrared spectroscopy (FT-IR) measurements were performed on a spectrometer using the attenuated total reflectance (ATR) sampling method (FT/IR-6600, Jasco). Thermogravimetric analysis (TGA) combined with differential scanning calorimetry (DSC) was conducted on a thermal analysis system (LabSys Evo 1600 TGA, SETARAM) under dry airflow and in the temperature range of 25–800 °C at a constant rate of 5 °C min^{-1}. ^{1}H-NMR and ^{13}C-NMR spectra were collected using an NMR spectrometer (AVANCE Neo 600 MHz, Bruker). Chromatographic measurement of the 4,8-dihydroxynapthalene-2,6-dicarboxylic acid linker was carried out on a chromatograph system (Acquity UPLC® H-Class Plus, Waters) with the Acquity UPLC®BEH C18 column (1.7 μm, 2.1 × 50 mm). This system was incorporated with a Waters SQ Detector for mass spectroscopy (MS) and controlled by Masslynx V4.2 software. X-ray photoelectron spectroscopy (XPS) was analyzed using an X-ray photoelectron spectrometer (PHI 5000, Chigasaki) with a monochromatic Al K_α source operating at 50 W and 15 kV. The N_2 adsorption isotherm was performed using a surface characterization analyzer (3Flex, Micromeritics). Raman spectroscopy was collected using a spectrometer (XploRA One 532 nm, Horiba). Scanning electron microscopy (SEM) image was measured using a microscope (FESEM S-4800, Hitachi) with an accelerating voltage of 10 kV incorporated with energy-dispersive X-ray (EDX) mapping recorded on an instrument (EDX H-7593, Horiba). Transmission electron microscopy

(TEM) was conducted using a microscope (Jeon 1010, Hitachi) with a high voltage of 80 kV. An atomic absorption spectrophotometer (AAS) was performed using a spectrometer (iCE 300 Series, Thermo Scientific) to quantify the Pb^{2+} ion with an absorption wavelength of 217 nm.

Synthesis of 4,8-dihydroxynapthalene-2,6-dicarboxylic acid ($H_2NDC(OH)$) linker

According to a previously published procedure,[44,45] a mixture of H_4SNDC linker (0.300 g, 0.798 mmol) and NaOH (0.750 g, 18.8 mmol) was well-mashed in a crucible and then heated at 350 °C with a rate of 5 °C per min for 90 min. At the end of the reaction, the mixture was cooled to room temperature, then dissolved in distilled water, filtered, and precipitated by adding excess concentrated HCl (37 wt%, 120 mL). A bright yellow product was collected, washed with acetonitrile, and dried upon vacuum for 12 h at 70 °C. ^{1}H-NMR (DMSO-d_6, 600 MHz): δ = 10.75 (s, 2H); 8.28 (s, 2H); and 7.43 ppm (s, 2H) (Fig. S1, ESI†). ^{13}C-NMR (DMSO-d_6, 600 MHz): δ = 167.47 (s, 2C); 154.36 (s, 2C); 129.32 (s, 2C); 127.06 (s, 2C); 115.27 (s, 2C); and 107.93 ppm (s, 2C) (Fig. S2, ESI†). ESI(−) MS (1000 ppb, cone voltage of 30 V): m/z = 247.02) (Fig. S3, ESI†).

Synthesis of HCMUE-2 material

A mixture of $ZrOCl_2{\cdot}8H_2O$ (0.0393 g, 0.122 mmol) and $H_2NDC(OH)_2$ (0.0327 g, 0.132 mmol) was ultrasonically dissolved in a 20 mL Pyrex vial containing DMF solvent (6 mL) and formic acid (1.5 mL) for 15 min. Then, the mixture was heated at 120 °C for 72 h. After cooling to room temperature, the sample was centrifuged and washed with DMF for 48 h (20 mL) and methanol for 48 h (20 mL). During the solvent exchange, each solvent was decanted and refilled four times per day. The brown product was dried and evacuated under vacuum at 120 °C for 24 h to yield the brown guest-free sample, denoted as HCMUE-2 (80% yield, based on Zr^{4+}).

Batch adsorption investigations

All the experiments were conducted at room temperature with a constant stirring rate and repeated at least three times for further tests. To demonstrate the effect of the pH value on the adsorption ability, 250 mg L^{-1} of Pb^{2+} (100 mL) was selected as the initial concentration with 10 mg of HCMUE-2 after stirring for 24 h. The pH range from 1 to 5.5 was adjusted by 0.01 M HNO_3 and 0.01 M NaOH solutions with a pH meter to avoid the generation of precipitation states of Pb^{2+}.[46–48] The content of the material was carefully surveyed with an optimal pH studied previously. In detail, the dosage (2–25 mg) of HCMUE-2 was introduced to 100 mL of the Pb^{2+} solution with an initial concentration of 100 mg L^{-1} at an optimal pH value. Herein, the concentration of Pb^{2+} was determined using the atomic absorption spectroscopy (AAS) method after appropriate adsorption intervals with a calibration curve derived from the standard solutions (Fig. S4, ESI†). The adsorption capacity (mg g^{-1}) at t (q_t) and equilibrium (q_e) times as well as the removal percentage (R%) were respectively calculated by applying eqn (1)–(3):

$$q_t = \frac{(C_o - C_t)V}{m} \quad (1)$$

$$q_e = \frac{(C_o - C_e) \times V}{m}, \quad (2)$$

$$R(\%) = \frac{C_o - C_t}{C_o} \times 100, \quad (3)$$

where C_o, C_t, and C_e (mg L^{-1}) are the concentrations of Pb^{2+} at initial, t and equilibrium times, respectively. V (mL) and m (mg) are the solution volume and a certain amount of adsorbent, respectively.

Next, the adsorption isotherms of the Pb^{2+} adsorption over HCMUE-2 were conducted. Accordingly, 15 mg of HCMUE-2

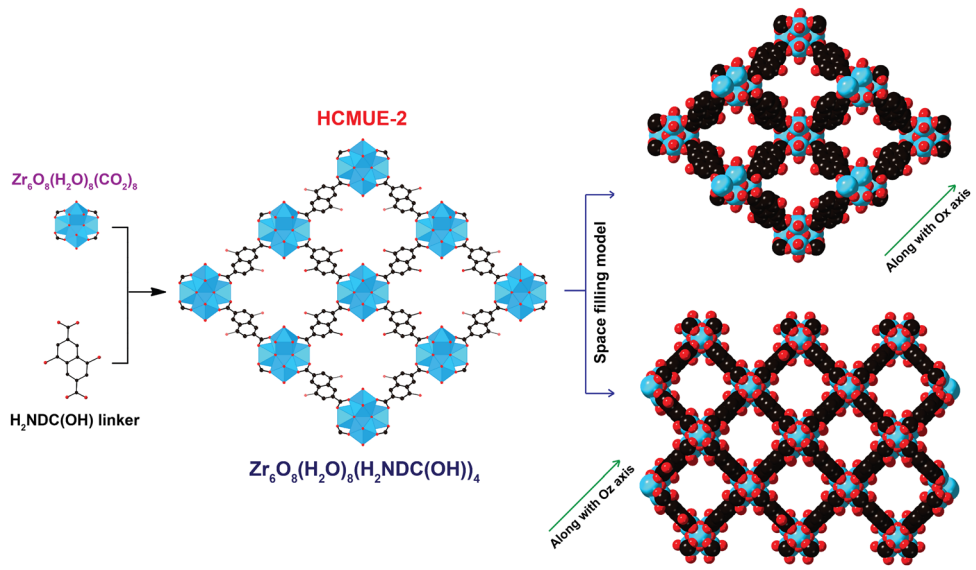

Fig. 1 Structure of the HCMUE-2 backbones is constructed from the $Zr_6O_8(H_2O)_8(CO_2)_8$ SBUs with $H_2NDC(OH)$. Atom colors: Zr polyhedra, blue; C, black; O, red. All H atoms are omitted for clarity.

was added to 100 mL of the Pb^{2+} solution with a concentration range of 50–1000 mg L^{-1} at pH = 5.5 and stirred for 24 h. The remaining concentrations of Pb^{2+} in each solution were determined.

To investigate the adsorption kinetics of Pb^{2+}, HCMUE-2 (5 mg) was introduced to 50 mL of the Pb^{2+} solution (50 mg L^{-1}) at pH = 5 and stirred at various intervals from 1 to 60 min. Noteworthily, the dosage and pH value are chosen to be 5 mg and 5, respectively, to observe the kinetics because the adsorption rate of HCMUE-2 is fast at dosages over 5 mg and pH = 5.5, causing incorrect analyses in a short time.

Recycling experiments

To test the reusable ability of HCMUE-2, regeneration was performed by immersing the material in a 1% HNO_3 solution as the desorption solvent upon stirring for 24 h. Herein, to prove the complete desorption of Pb^{2+} from HCMUE-2, filtration after the soaking process was checked without the Pb^{2+} trace found in the AAS spectrum. Continuously, the sample was collected by centrifugation, washed with distilled water until pH = 7, and exchanged in MeOH for 48 h (15 mL per 24 h). The solid was then centrifugated, activated at 120 °C upon vacuum for 24 h, and utilized for the following adsorption studies.

3. Results and discussion

Full characterization of hydroxyl-modified Zr-based MOFs

To evaluate the influence of hydroxyl groups within the backbone of the material on the Pb^{2+} adsorption performance, we fabricated two Zr-based MOF materials with the same structure,

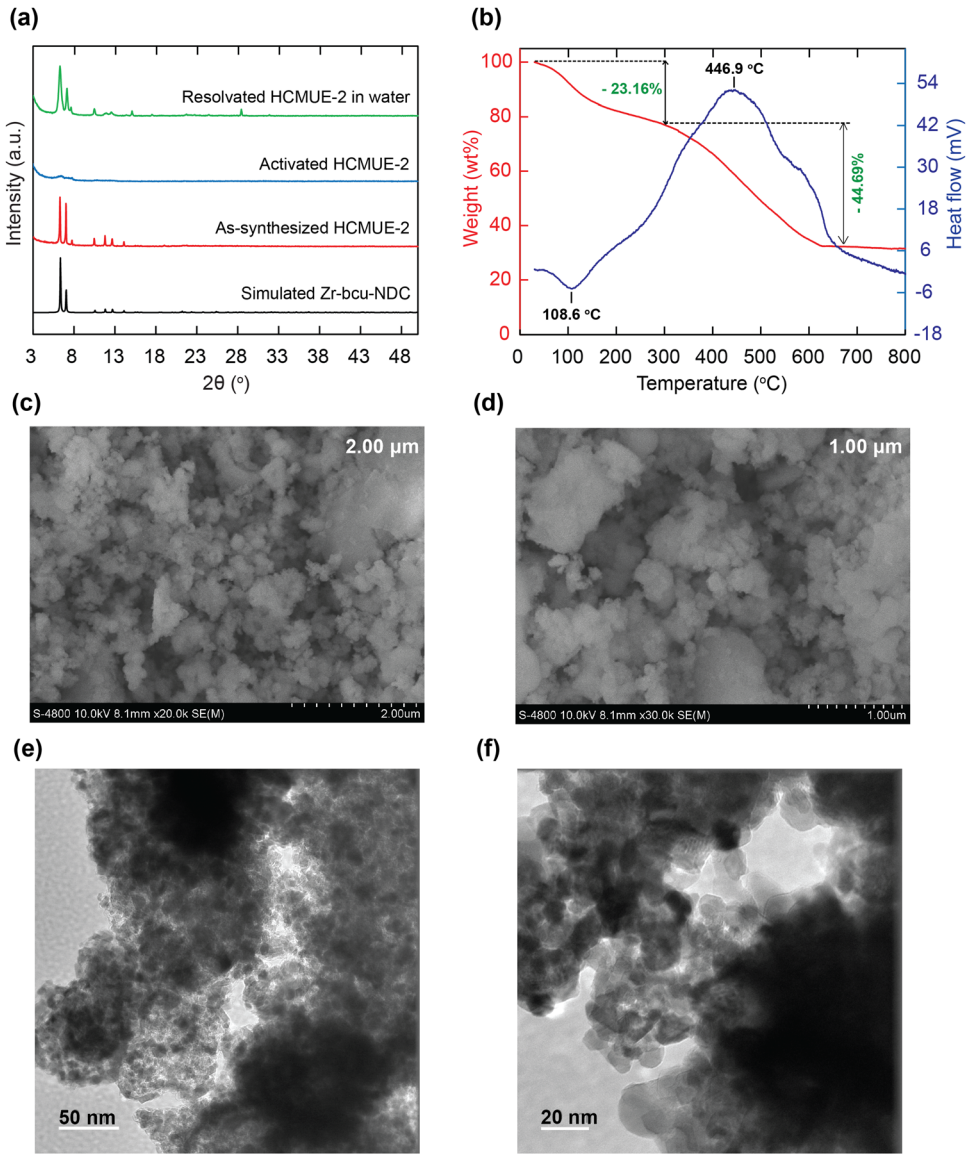

Fig. 2 Powder X-ray diffraction analysis of as-synthesized HCMUE-2 (red), activated HCMUE-2 (blue), resolvated HCMUE-2 immersed in water (green) compared with the simulated Zr-bcu-NDC (black) (a); TGA diagram (red) and DSC curve (blue) of activated HCMUE-2 (b); SEM images of HCMUE-2 at various scale bars of 2.00 µm (c), and 1.00 µm (d); TEM images of activated HCMUE-2 at different scale bars of 50 nm (e), and 20 nm (f).

namely Zr-bcu-NDC and HCMUE-2. The architectures of Zr-bcu-NDC and HCMUE-2 are clearly depicted by the incorporation of organic linkers, such as NDC^{2-}, $NDC(OH)^{2-}$, and $Zr_6O_8(H_2O)_8(-COO)_8$ SBUs (Fig. 1 and Fig. S5, ESI†). Consequently, the Zr-bcu-NDC material was prepared by combining $ZrOCl_2{\cdot}8H_2O$ salt and a non-OH-functionalized H_2NDC linker in DMF.[49] Meanwhile, HCMUE-2 was fabricated from $ZrOCl_2{\cdot}8H_2O$ salt and OH-rich $H_2NDC(OH)$ linker in DMF in the presence of formic acid as a modulator to form a three-dimensional structure with bcu topology, similar to the Zr-bcu-NDC backbone (Fig. 1). Notably, HCMUE-2 adopts the densely packed –OH moieties within the backbone, leading to the efficient enhancement of the interaction with the positively charged Pb^{2+} species *via* the electron transport process from the unpaired electrons of oxygen atoms on the –OH groups to the empty d orbitals of Pb^{2+}. The phase purity of HCMUE-2 is confirmed by PXRD measurement (Fig. 2a), which is in good accordance with the simulated structure of Zr-bcu-NDC. Nevertheless, the activated HCMUE-2 sample has a poor structural order with almost imperceptible diffraction peaks because of the high flexibility of the hydroxyl moieties inside the MOF structure after activation. This can be accounted for by the release of guest solvents, which strongly interact with the hydroxyl groups through a hydrogen bonding system, from the MOF structure, driving the loss of architectural order. Interestingly, the crystallinity recovered after soaking in water (Fig. 2a). This is also affirmed by the N_2 adsorption isotherm at 77 K of the HCMUE-2 material. Accordingly, the value of the surface area (BET) of the activated HCMUE-2 is much smaller than that of the theoretical data. This situation is observed in the previously published works.[37,40] Next, Raman spectra of HCMUE-2 and $H_2NDC(OH)$ linker are indicated in Fig. S6 (ESI†). The new signals located at 1364, 1418, and 1583 cm^{-1} are related to the characteristic bands of C═O and C═C, respectively, in the HCMUE-2 material but shifted to other frequency ranges for the $H_2NDC(OH)$ linker. Particularly, the vibrational mode of the Zr–O bond appeared at 564 cm^{-1} in the HCMUE-2 spectrum. In addition, the FT-IR spectra of $H_2NDC(OH)$ and HCMUE-2 are illustrated in Fig. S7 (ESI†). In detail, the new signals that emerged at 639, 1426, and 1599 cm^{-1} represent the vibrations of Zr–O, symmetric C–O, and asymmetric C–O, respectively, which appear in the HCMUE-2 spectrum but are absent in the $H_2NDC(OH)$ spectrum. Additionally, the vibrational modes originating from C═C stretching at 1554 cm^{-1} and aromatic O–H bending at 1365 cm^{-1} are present in both samples.

To further confirm the thermal and architectural robustness of HCMUE-2, a TGA-DSC diagram was performed on the activated sample under dry air (20% O_2 and 80% N_2). In detail, the weight loss of 23.16 wt% in the first stage can be ascribed to the release of the absorbable surface and coordinated water molecules in the HCMUE-2 cavities from room temperature to 300 °C, corresponding to a specific endothermic peak at 108.6 °C. The second stage, with a significant weight loss (44.69 wt%) from 300 to 600 °C, can be assigned to the decomposition of the MOF framework with an exothermic peak at 446.9 °C to form the final product as ZrO_2 residue

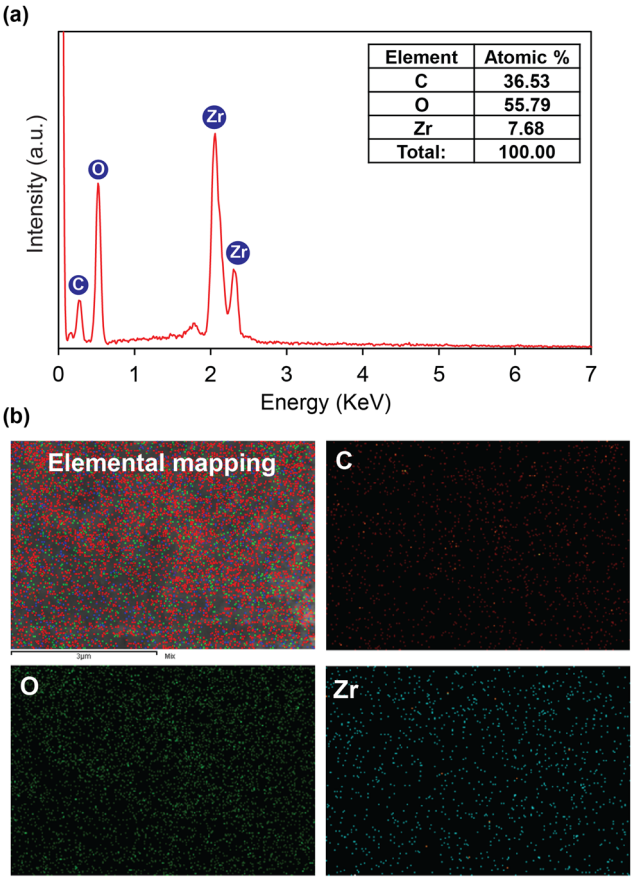

Fig. 3 EDX spectrum of activated HCMUE-2 (a); elemental mapping by SEM-EDX of activated HCMUE-2 (b).

(31.47 wt%) (Fig. 2b). Consequently, the HCMUE-2 architecture is determined to be thermally up to 300 °C. This reveals that HCMUE-2 possesses promising properties for many practical applications. The morphology of HCMUE-2 is recorded by the SEM and TEM images (Fig. 2c–f), which display that the morphologies of HCMUE-2 are prism-like particles with high agglomeration and possess an average size of 15–20 nm. In addition, the EDX-mapping spectrum of HCMUE-2 is indicated in Fig. 3. Accordingly, the complete distribution of the C, O, and Zr elements in HCMUE-2 shows the successful synthesis of the material at a high single-phase level. Furthermore, the XPS analysis exhibits the uniform presence of the elements (C, O, and Zr) inside the HCMUE-2 sample (Fig. 4a). High-resolution spectra were employed to prove the constituents on the surface of HCMUE-2 (Fig. 4b–d). Consequently, the C 1s curve displays the peaks at 283.8 eV, 285.2 eV, 286.0 eV, and 287.5 eV, which are attributed to the bonds of C═C/C–C, C–O, C═O, and COO–, respectively, within the MOF material.[50,51] The O 1s spectrum can be deconvoluted into three peaks at 529.1 eV, 530.9 eV, and 531.7 eV, relating to the Zr–O–Zr, C–O, and Zr–O–H, respectively.[52,53] These gained data are similar to the mentioned Raman and FT-IR spectra. Notably, the Zr spectrum can be divided into peaks at 181.6 eV and at 184.0 eV, which are assigned to the Zr $3d_{5/2}$ and Zr $3d_{3/2}$, respectively.[54] All the

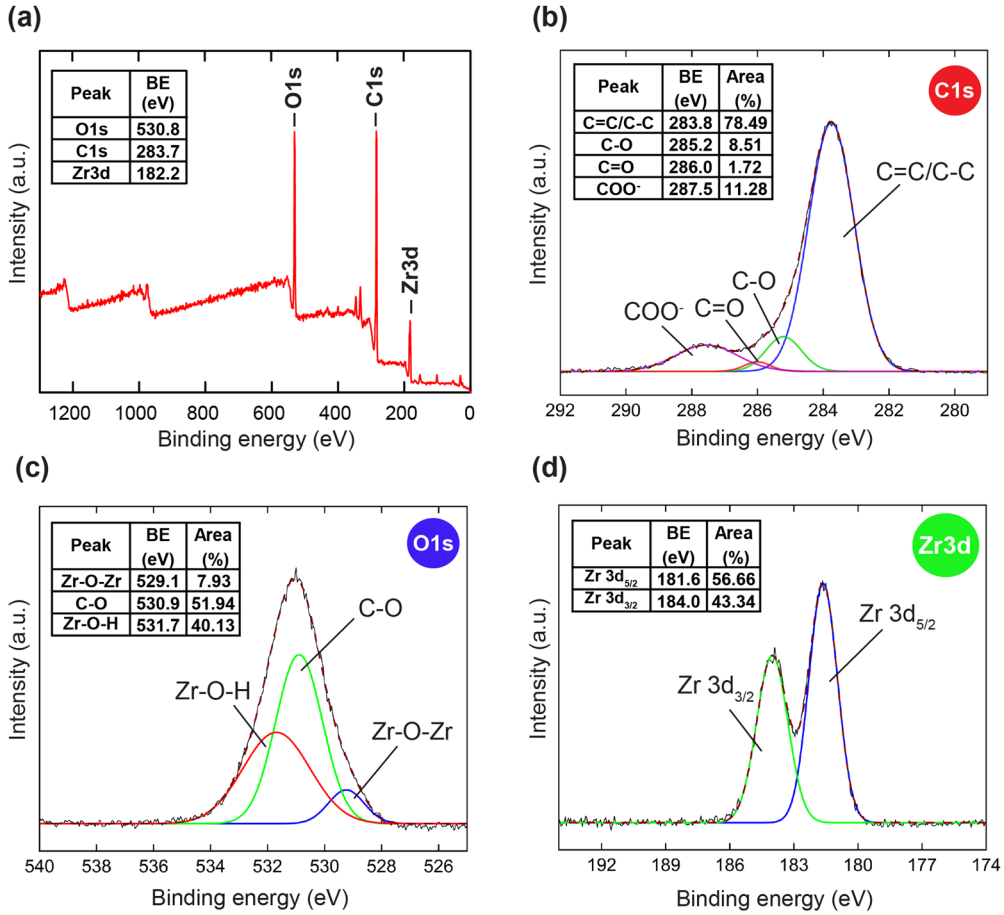

Fig. 4 XPS measurement of HCMUE-2: the XPS survey of HCMUE-2 (red) (a); high-resolution spectrum of C 1s in HCMUE-2 (b); high-resolution spectrum of O 1s in HCMUE-2 (c); and high-resolution spectrum of Zr 3d in HCMUE-2 (d).

above affirmations, gained from PXRD, Raman, FT-IR, TGA-DSC, SEM-EDX-mapping, TEM, and XPS analyses, reveal that HCMUE-2 is successfully fabricated with extraordinary properties for real-life situations.

To gain insight into the effect of the amount of hydroxyl groups inside HCMUE-2 on the Pb^{2+} adsorption ability, a series of uptake investigations were conducted. In detail, 10 mg of each material was added to 100 mL of the Pb^{2+} solutions with different initial concentrations (50–500 mg L^{-1}) at pH = 5. As a result, the Pb^{2+} uptake capacities of Zr-bcu-NDC and HCMUE-2 are 54.7 and 740.5 mg g^{-1}, respectively, at an initial Pb^{2+} concentration of 500 mg L^{-1} (Fig. 5a). It is noteworthy that the Zr-bcu-NDC material displays a poor adsorption capacity for Pb^{2+} due to the absence of –OH moieties within the framework, whereas the significant increase in the Pb^{2+} uptake onto HCMUE-2 can be explained by the dense distribution of hydroxyl groups within the backbones of HCMUE-2, resulting in the formation of robust chemical bonding between the hydroxyl moieties and Pb^{2+} *via* the convenient electron transfer from unpaired electrons of oxygen atoms to the Pb^{2+} d orbitals.

Effects of pH and adsorbent dose

The solution pH value is considered essential in evaluating the generation of the charged moieties within the material. Thus, investigations were conducted to determine the pH point of zero charge (pH_{pzc}) of HCMUE-2 (Fig. S8, ESI†). Accordingly, the HCMUE-2 material possesses a pH_{pzc} value of 4.2. It is interesting to note that the surface charge of the material could change around pH_{pzc}. Subsequently, the solution pH regions from 1 to 7 were performed to inspect the considerable dependence of the pH values on the Pb^{2+} uptake over HCMUE-2 (Fig. 5b). Consequently, a poor uptake level of Pb^{2+} is exhibited in the pH ranges from 1 to 4 ($< pH_{pzc}$). This can be attributed to the protonation process of hydroxyl groups on the linkers and μ-OH moieties located at the clusters in MOFs, driving the internal and external channel walls of HCMUE-2 to turn more positively charged species. They can generate remarkable repulsion forces between the copious H^+ ions, positively charged forms within HCMUE-2, and the Pb^{2+} species from the solution.[46,55] Interestingly, with the pH regions from 5 to 5.5 ($> pH_{pzc}$), the Pb^{2+} adsorption capacity significantly increases compared with the low pH values. Herein, the negatively charged moieties within HCMUE-2 formed by the deprotonation of –OH groups at higher pH ranges effectively interact with the Pb^{2+} ions *via* electrostatic attraction and sharing electron mechanism to create the stable complexation of Pb–O. It is important to note that the hydroxide precipitation forms of the Pb^{2+} ions can be generated at the pH range to be greater than or

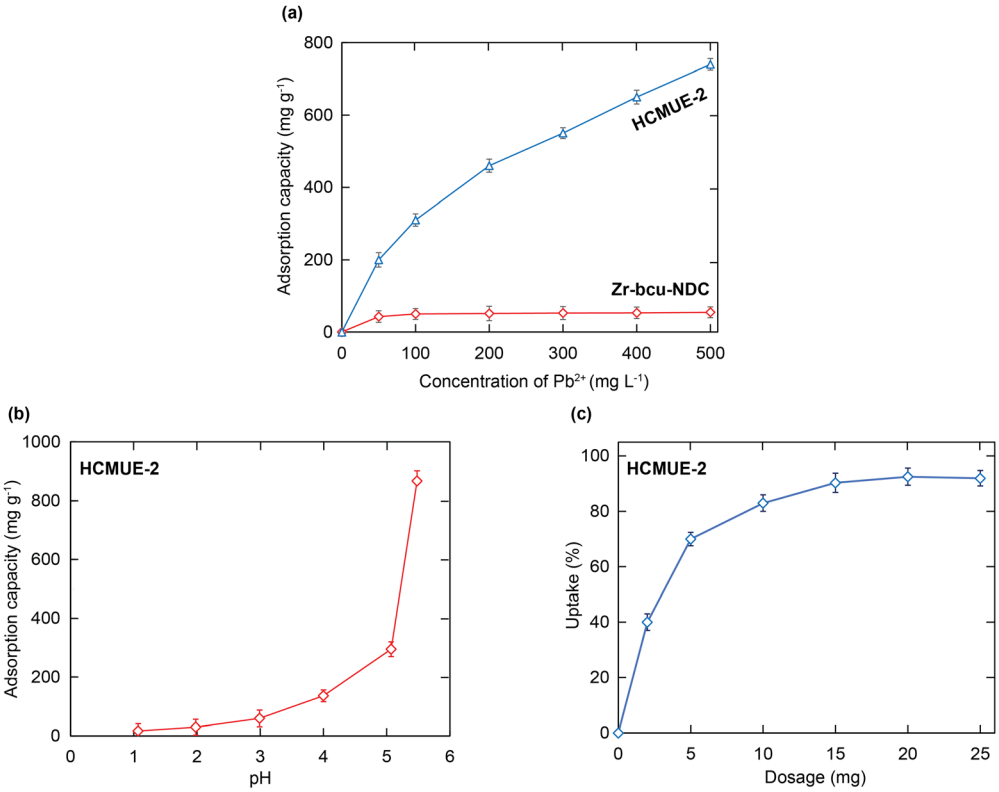

Fig. 5 Effect of the amount of hydroxyl groups in the architectures of Zr-bcu-NDC and HCMUE-2 on their Pb^{2+} uptake capacity [m = 10 mg, V = 100 mL, C_o: 50–500 mg L^{-1}, t = 24 h, and pH = 5] (a); influence of solution pH on the Pb^{2+} adsorption capacity over HCMUE-2 with an initial Pb^{2+} concentration of 250 mg L^{-1} capacity [m = 10 mg, V = 100 mL, C_o = 250 mg L^{-1}, t = 24 h, and pH = 1–5.5] (b); influence of MOF dosage on the Pb^{2+} removal capacity [m = 2–25 mg, V = 100 mL, C_o = 100 mg L^{-1}, t = 24 h, and pH = 5.5] (c).

equal to 6,[46–48] which detaches from the solution and causes the obstacles to confirm whether adsorption or precipitation appeared. Therefore, we select the optimal pH value of 5.5 to conduct the subsequent adsorption experiments.

To assess the ideal dosage of adsorbent used for the Pb^{2+} elimination, various doses of the HCMUE-2 material from 2 to 25 mg were studied during the adsorption process of Pb^{2+} at pH = 5.5. As depicted in Fig. 5c, the removal of Pb^{2+} rapidly increased from 61.7% to 91.2% as the adsorbent dosage rose from 2 to 25 mg. This improvement can be attributed to the higher content of HCMUE-2, which led to an increase in more active sites and pores for the Pb^{2+} uptake. As the material content reaches about 15–25 mg, the adsorption uptake of Pb^{2+} is recorded with no significant change, indicating that the adsorption equilibrium has been established. Therefore, the optimum adsorbent dosage of 15 mg is chosen for the following studies.

Adsorption isotherms

For a more detailed explanation of the adsorption essence between HCMUE-2 and the Pb^{2+} ions, isothermal adsorption experiments were studied. It is found that a significant increase in the adsorption capacity was recorded with an increase in Pb^{2+} initial concentration from 50 to 1000 mg L^{-1} (Fig. 6a). The maximum Pb^{2+} adsorption capacity (q_m) of HCMUE-2 is 1115.9 mg g^{-1}. This is attributed to the presence of densely packed adsorption regions within HCMUE-2, leading to a considerable enhancement of electrostatic attraction and donor–acceptor electron transport between the hydroxyl active sites and Pb^{2+} species. The obtained data show that the essential active sites of HCMUE-2 are the inhibition components for the Pb^{2+} removal.

To further explore the uptake process, the models of Langmuir, Freundlich, Temkin, Dubinin–Radushkevich (DR), and separation factor (R_L) were employed to admit the adsorption mechanism onto HCMUE-2. The non-linear types of the mentioned models and R_L values are clearly displayed in the following eqn (4)–(8):

$$q_e = \frac{q_m \cdot K_L \cdot C_e}{1 + K_L \cdot C_e}, \quad (4)$$

$$q_e = K_F \cdot C_e^{1/n}, \quad (5)$$

$$q_e = \frac{RT}{b} \ln(k_T C_e) \quad (6)$$

$$q_e = q_m \cdot e^{-K_{DR} \cdot \varepsilon^2}, \quad (7)$$

$$R_L = \frac{1}{1 + K_L C_o}, \quad (8)$$

where q_e (mg g^{-1}), C_e (mg L^{-1}), and q_m (mg g^{-1}) are the Pb^{2+} adsorption capacity, the concentration at equilibrium and the theoretical maximum capacity of Pb^{2+}, respectively.

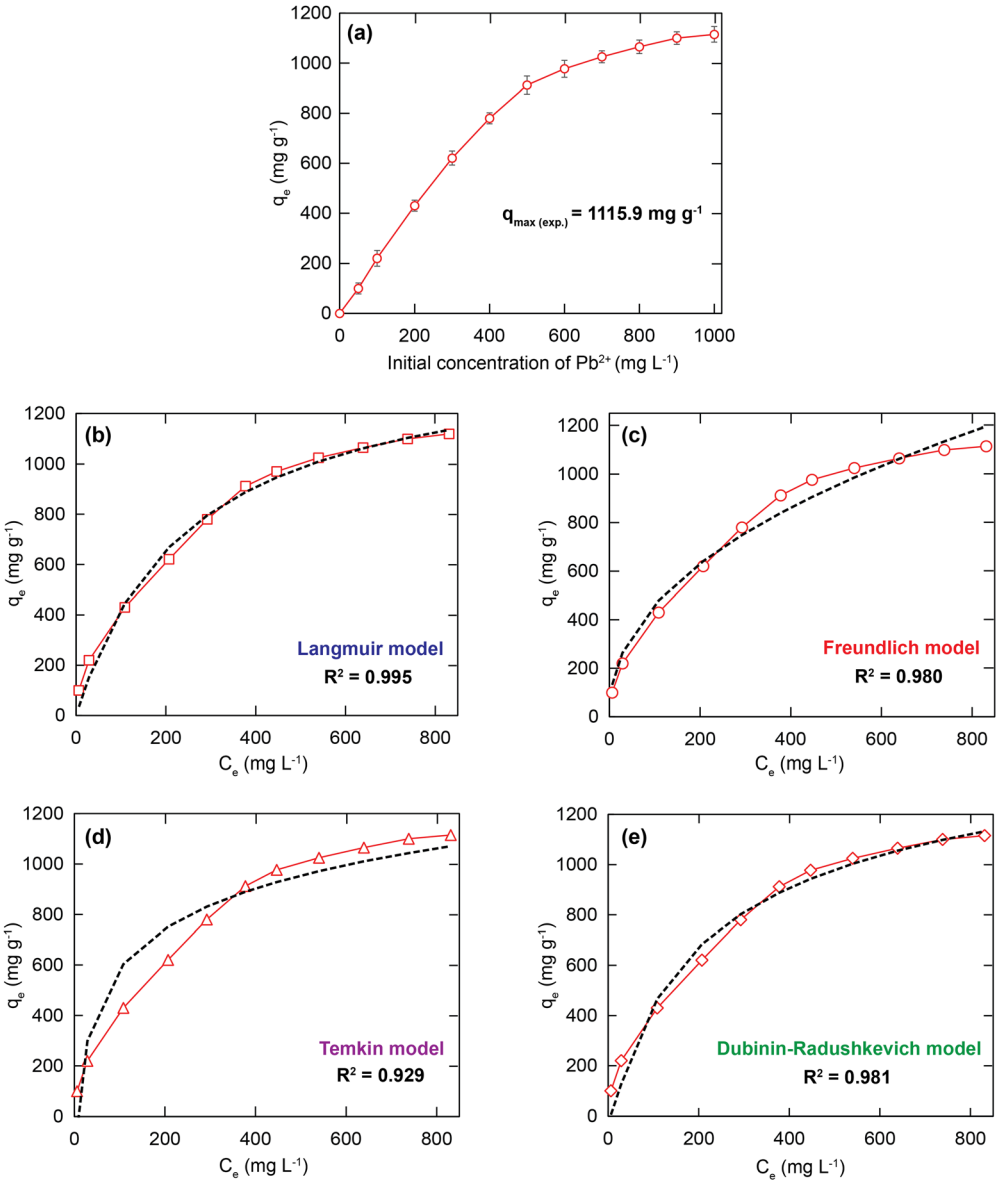

Fig. 6 Effect of the initial concentration of Pb^{2+} on the adsorption capacity of HCMUE-2 capacity [m = 15 mg, V = 100 mL, C_o: 50–1000 mg L^{-1}, t = 24 h, and pH = 5.5] (a); data fitting with the adsorption isotherm models: Langmuir (b), Freundlich (c), Temkin (d), and Dubinin–Radushkevich (e).

K_L (L mg^{-1}), K_F (mg g^{-1} (L $g^{-1})^{1/n}$), K_T (L mg^{-1}), and K_{DR} (mg g^{-1}) represent the constants of Langmuir, Freundlich, Temkin, and DR, respectively. The $1/n$ and ε values represent the adsorption capacity index of the Freundlich isotherm and the constant of the DR model, respectively. The R, T, and b values are the constant of gas, the temperature in Kelvin, and the adsorption heat in the Temkin model, respectively.

As illustrated in Fig. 6b–e and Table 1, the non-linear plots of the aforementioned models for the removal of Pb^{2+} over HCMUE-2 are elucidated. The obtained results indicate that the equilibrium parameters fitted by applying the Langmuir model are greater than those of the remaining models. In detail, the non-linear fitting coefficients of the Freundlich (R^2 = 0.980), Temkin (R^2 = 0.929), and DR (R^2 = 0.981) models are much lower than those of the Langmuir model (R^2 = 0.995). Additionally, the theoretical Pb^{2+} adsorption capacity (q_m) is 1309.3 mg g^{-1}, which is relatively close to the experimental capacity (1115.9 mg g^{-1}). Based on the achievable data, it is proposed that the adsorption of Pb^{2+} onto HCMUE-2 appears only as an adsorption layer of Pb^{2+} formed at the boundary of the active regions within HCMUE-2. Furthermore, the separation value (R_L) determined from the Langmuir model plays an important role in evaluating the convenience of the uptake process. Accordingly, the R_L factor shows the value to be smaller than 1 and larger than 0, implying that the Pb^{2+} removal over HCMUE-2 is a chemical adsorption process. This can be depicted by the electrostatic attraction and electron transfer between the cationic Pb^{2+} ions and hydroxyl active sites inside HCMUE-2. This phenomenon has also been observed in previously reported works.[40,46]

Table 1 Fitting data calculated from the Pb^{2+} uptake isothermal models onto HCMUE-2

Isotherm models	Parameters	Value
Langmuir	q_m (mg g^{-1})	1309.3
	K_L (L mg^{-1})	0.0040
	R^2	**0.995**
Freundlich	$1/n$	0.449
	K_F (mg g^{-1} (L $g^{-1})^{1/n}$)	58.409
	R^2	**0.980**
Temkin	b	10.891
	K_T (L mg^{-1})	0.129
	R^2	**0.929**
DR	K_{DR} (mg g^{-1})	0.290
	R^2	**0.981**

Adsorption kinetics

To understand the relationship between adsorption ability and contact time, further adsorption kinetic experiments were conducted. Herein, to prevent imprecise measurements in short-time contact intervals due to the rapid removal rate of HCMUE-2, the MOF content of 5 mg and the solution pH value of 5 were used. As a consequence, the Pb^{2+} uptake rate onto HCMUE-2 increases promptly during the original 10 min because of the great number of available adsorption sites at the original periods. It gains the adsorptive equilibrium level after 20 min (Fig. 7a). It is observed that the rapid removal of Pb^{2+} over HCMUE-2 is a promising point to cope with the stated

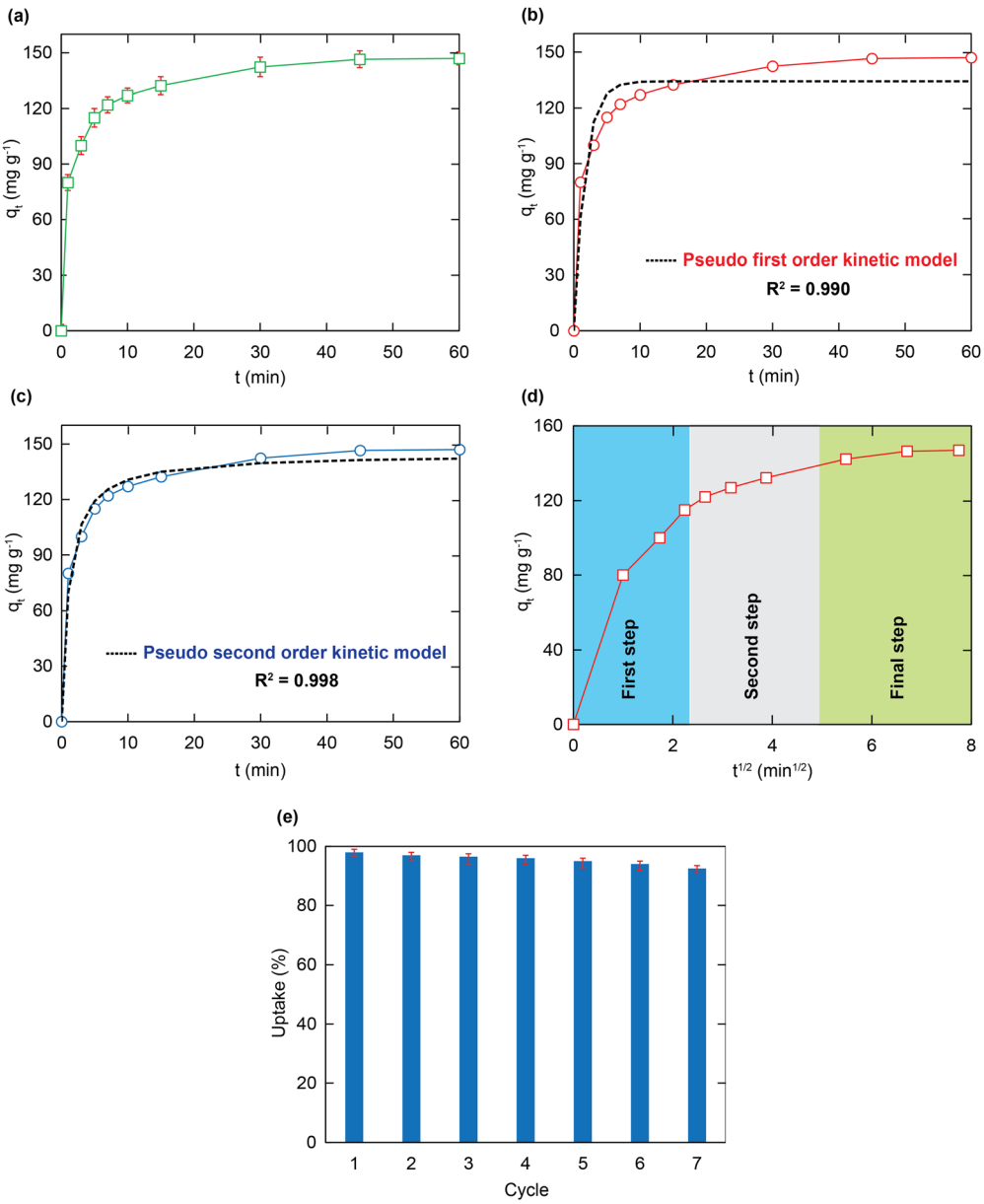

Fig. 7 Kinetic data for the Pb^{2+} adsorption onto HCMUE-2 capacity [m = 5 mg, V = 50 mL, C_o: 50 mg L^{-1}, t = 1–60 min, and pH = 5] (a), fitting results with the adsorption kinetic models: pseudo-first-order (b), pseudo-second-order (c), and intra-particle diffusion model (d). Regenerration of HCMUE-2 in the Pb^{2+} uptake (e).

Table 2 Parameters of the adsorption kinetics of Pb^{2+} onto HCMUE-2

Kinetic models	Paramaters	Value
Pseudo first order	$q_{e,exp}$ (mg g^{-1})	147.2
	$q_{e,cal}$ (mg g^{-1})	134.3
	k_1 (min^{-1})	0.606
	R^2	**0.990**
Pseudo second order	$q_{e,cal}$ (mg g^{-1})	144.7
	k_2 (g mg^{-1} min^{-1})	1629.8
	R^2	**0.998**

disadvantages of the traditional materials, thereby opening the potential applications of HCMUE-2 for the treatment of heavy metal ions in practical environments. The truth reveals that the diffusion rate and interactions are vital criteria for identifying the adsorption performance of HCMUE-2. Thus, the kinetic models of pseudo-first-order, pseudo-second-order, and intra-particle diffusion (eqn (S1)–(S3), ESI†) were utilized to demonstrate the adsorption mechanism of Pb^{2+}. As shown in Fig. 7b and c and Table 2, it can be observed that the non-linear fitting coefficient of the pseudo-first-order model (R^2 = 0.990) is smaller than that of the pseudo-first-order model (R^2 = 0.998). Particularly, the experimental Pb^{2+} adsorption capacity (147.2 mg g^{-1}) is much closer to the theoretical value (144.7 mg g^{-1}). Hence, the Pb^{2+} uptake over HCMUE-2 is chemical adsorption performed by the electron exchange or sharing to form a strong interaction between the positively charged Pb^{2+} ions and hydroxyl-containing moieties within MOF.

Remarkably, the removal process of Pb^{2+} onto HCMUE-2 can be clarified into three steps, as illustrated in Fig. 7d. Accordingly, in the first step, the Pb^{2+} ions diffuse rapidly from the solution to the external surface of the material until the surface is filled with guest species. In the second stage, the uptake rate is lower and attributed to the entry of the Pb^{2+} ions into the internal surface of HCMUE-2. In the final step, the Pb^{2+} ions travel sluggishly into the cavities and interact with the available active regions of the MOF until the adsorption equilibrium is accomplished. It is noteworthy that the third stage is the decision stage of the removal stage even though it is slow. This can be explained by the fact that the straight line does not go through the initial position.

Reusable investigation

The reusability of the absorbent is one of the important factors to consider in the economic efficiency of the material in terms of decreasing product costs. Herein, regeneration was addressed seven times with the experimental data, as illustrated in Fig. 7e. It is achieved that the uptake percentage

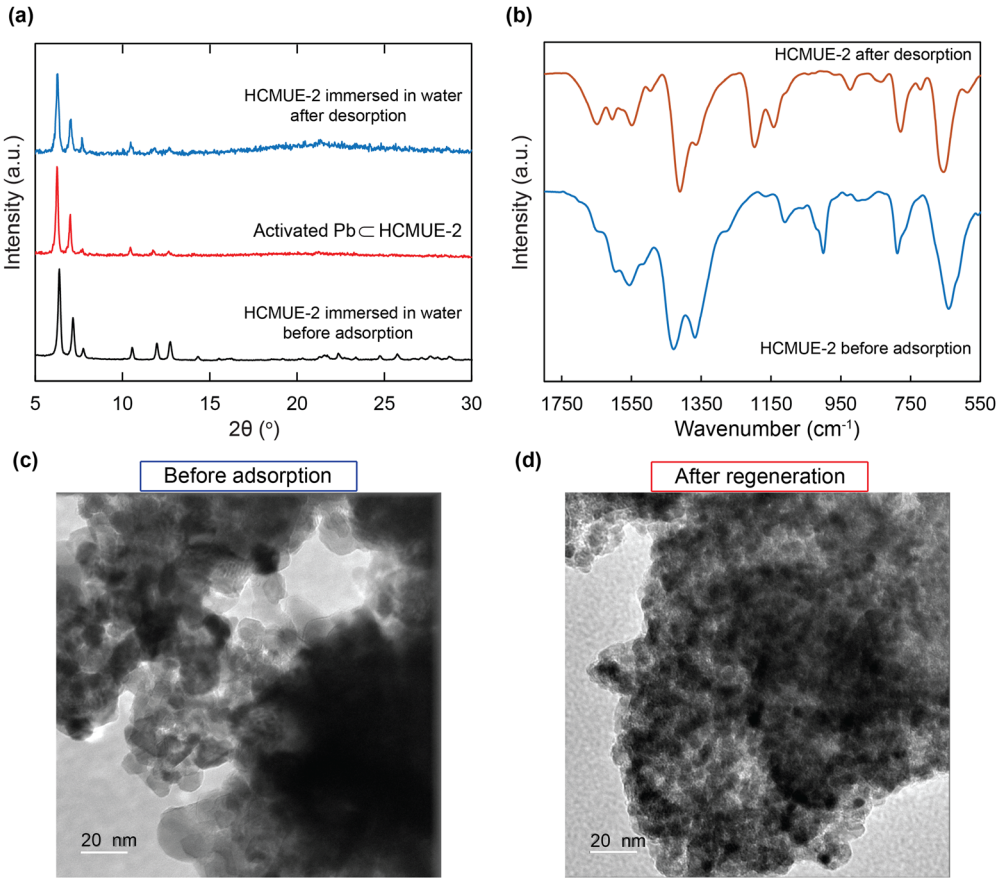

Fig. 8 PXRD pattern of HCMUE-2 before adsorption (black), and Pb⊂HCMUE-2 (red) compared to the PXRD pattern of HCMUE-2 after desorption (blue) (a); FT-IR spectrum of HCMUE-2 before adsorption (blue) and after desorption (brown) (b); TEM images of HCMUE-2 before adsorption (c) and after regeneration (d) at scale bar of 20 nm.

Table 3 The maximum uptake capacity of Pb^{2+} over HCMUE-2 compared to the other adsorbents

Material	q_{max} (mg g^{-1})	pH	Ref.
Active carbon	43.85	5.68	56
MoS_2biochar	189	5.0	57
Activated sludge	131.6	4.0	58
Tb-MOFs	547.0	5.5	46
MIL-101(Fe)/GO	128.6	6.0	59
MIL-101(Cr)-NH_2	88.0	6.0	60
UiO-66-$(COOH)_2$	420.2	4.8	61
O-TMU-40	215.0	6.5	62
TMU-5	251.0	10	62
$\{[Zn(ADB)L_{0.5}\ 1.5DMF]\}_n$	463.5	6.0	63
VNU-23	617.3	5.5	40
TMU-31	909.0	5.0	64
TMU-32	909.0	5.0	64
Zr-bcu-NDC	54.7	5.5	This work
HCMUE-2	1115.9		

reaches 93% after seven consecutive cycles. This shows the extraordinary advantages of HCMUE-2 in application on an industrial scale and in real-life situations.

Notably, the effective recycling of the HCMUE-2 material was evidenced by the PXRD, FT-IR, and TEM analyses. As depicted in Fig. 8a, the PXRD patterns of HCMUE-2 before and after the Pb^{2+} elimination show high agreement, proving the good architectural stability of HCMUE-2 after the removal. The FT-IR spectrum of HCMUE-2 after regeneration reveals that the vibrational signals in HCMUE-2 remain in comparison with the HCMUE-2 spectrum before adsorption (Fig. 8b). Furthermore, the surface morphology of the material is insignificantly different after recycling, as shown in Fig. 8c and d. These findings affirmed that HCMUE-2 could be used as a promising adsorbent in removing Pb^{2+} from wastewater.

To elucidate the dominant benefit of the HCMUE-2 material, the maximum uptake capacity of Pb^{2+} onto HCMUE-2 was compared with the other materials (Table 3). The obtained data show that HCMUE-2 has a much greater capacity than the other adsorbents. To the best of our knowledge, this value is one of the highest for the Pb^{2+} adsorption capacity compared to other porous materials. This demonstrates that the hydroxyl groups existing in the structure in terms of –OH moieties on the linker and in the clusters play an important role in the Pb^{2+} uptake.

Plausible adsorption mechanism: The unique adsorption property of Pb^{2+} over HCMUE-2 boosted us to obtain a deeper insight into the correlation between the Pb^{2+} species and hydroxyl moieties through additional measurements, including

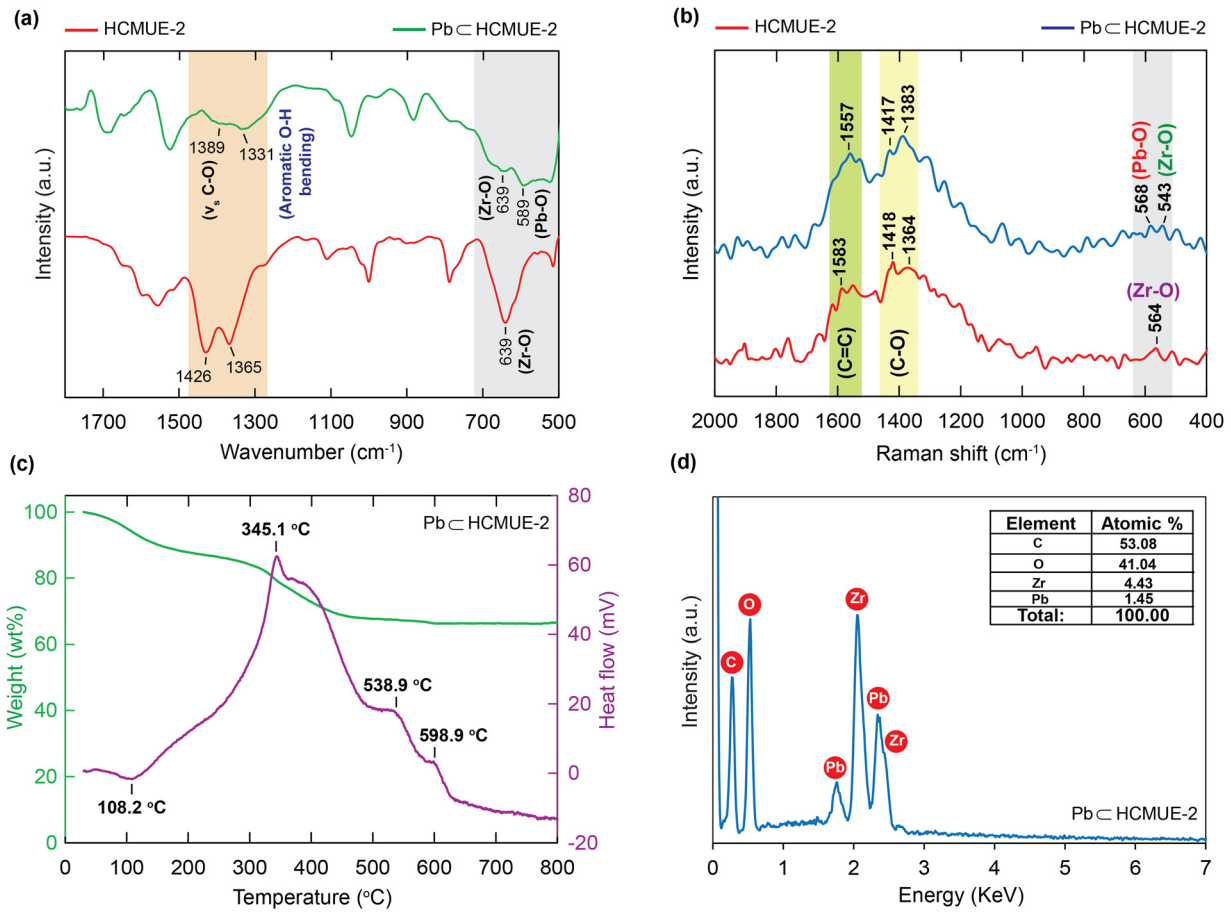

Fig. 9 FT-IR of Pb⊂HCMUE-2 (green) compared to HCMUE-2 (red) (a); Raman spectroscopy of Pb⊂HCMUE-2 (blue) in comparison with HCMUE-2 (red) (b); TGA-DSC curve of the Pb⊂HCMUE-2 sample (c); and EDX analysis for Pb⊂HCMUE-2 (d).

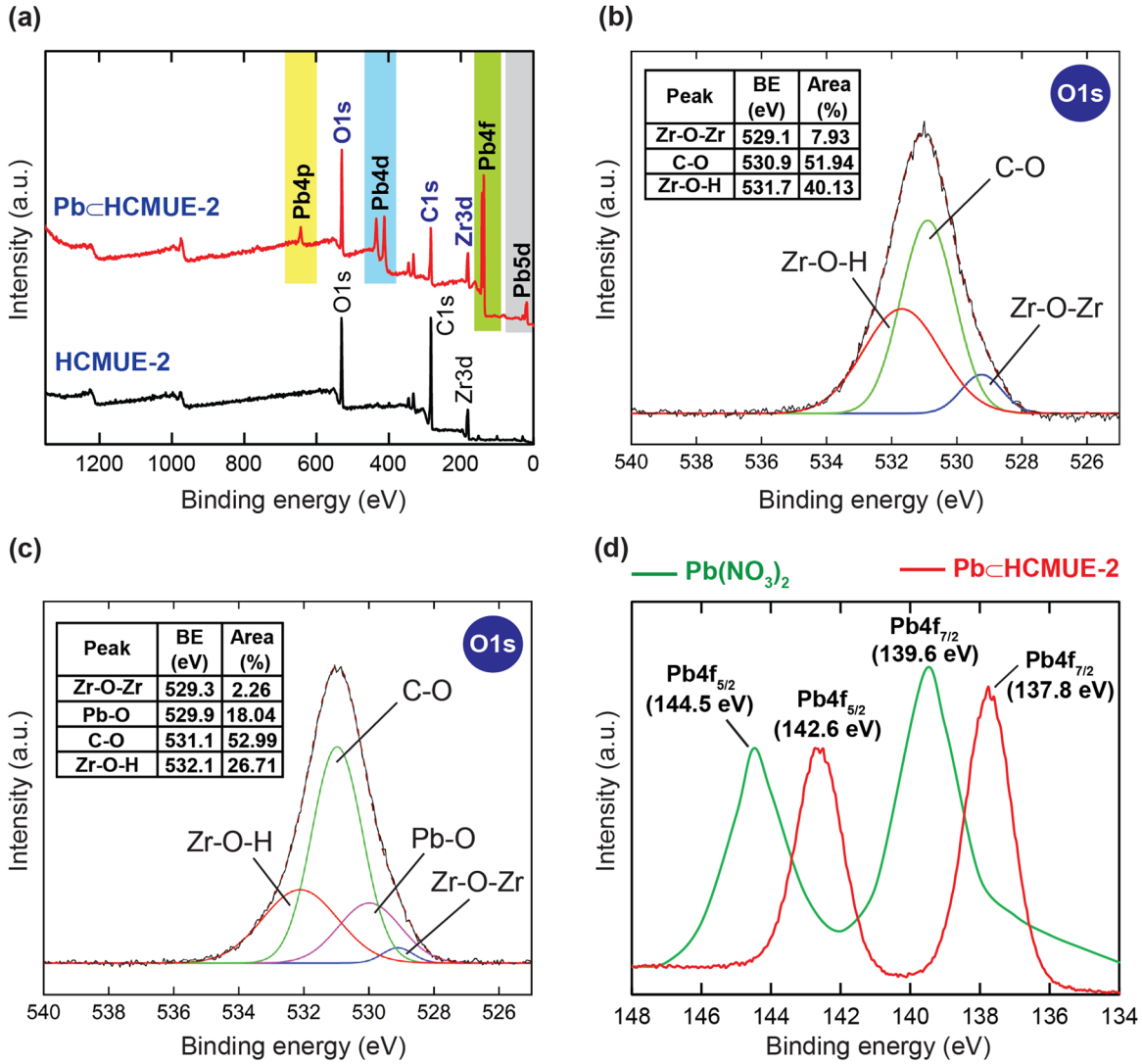

Fig. 10 The XPS analysis of HCMUE-2 before and after the Pb^{2+} removal: (a) the XPS survey; (b) high-resolution spectrum of O 1s in HCMUE-2; (c) high-resolution spectrum of O 1s in Pb⊂HCMUE-2; (d) the Pb 4f XPS spectra of Pb⊂HCMUE-2 (red) sample in comparison with pure $Pb(NO_3)_2$ solution (green).

FT-IR, Raman, TGA-DSC, EDX, and XPS analyses. It is observed that the FT-IR of Pb⊂HCMUE-2 reveals that the new absorption frequencies appeared at 1389, 1331, and 589 cm^{-1} features for the vibrations of C–O, O–H, and Pb–O, respectively, in HCMUE-2 (Fig. 9a). These observations confirm robust attraction, leading to the formation of stable chemical bonds between the oxygen atoms of the –OH groups and μ-OH in the clusters and Pb^{2+} and shifting the bonding vibrations to lower frequency ranges. This phenomenon is also found in the reported works.[38,40] Additionally, the Raman spectroscopy of Pb⊂HCMUE-2 was recorded and compared with the HCMUE-2 spectrum (Fig. 9b). The characteristic bands of C=C, C–O, Pb–O, and Zr–O move to different frequencies at 1557, 1417, 1383, 568, and 543 cm^{-1}, respectively, indicating the efficient incorporation of the Pb^{2+} ions onto the framework of HCMUE-2. To further confirm the appearance of Pb components in HCMUE-2 after uptake, the TGA-DSC curve of Pb⊂HCMUE-2 was performed, as illustrated in Fig. 9c. Consequently, there are two apparent exothermic peaks at 538.9 and 598.9 °C, which are assigned the oxidation of lead into PbO_2, but absent in the TGA-DSC diagram of HCMUE-2 (Fig. 2b). Remarkably, the weight percentage of the residue (66.17 wt%) for the Pb⊂HCMUE-2 sample is greater than the fresh HCMUE-2 material with the residue of 31.47 wt%. This is acceptable due to the remaining components of Pb⊂HCMUE-2 after annealing at 800 °C, involving the oxide compounds, such as ZrO_2 and PbO_2.[40] Subsequently, as shown in Fig. 9d, the EDS spectrum of Pb⊂HCMUE-2 indicates the emergence of new peaks confirmed as Pb signals appearing in HCMUE-2. These findings point to the existence of Pb moieties inside the backbone of HCMUE-2 after the removal process.

In particular, the uptake mechanism was further proved using the XPS procedure. As demonstrated in Fig. 10a, the XPS spectrum of Pb⊂HCMUE-2 shows the uniform presence of the

elemental components of C, O, and Zr, similar to the HCMUE-2 spectrum. Particularly, the new peaks originated at 643.1, 434.1, 413.2, 138.2, and 21.7 eV, corresponding to Pb 4p, Pb 4d, Pb 4f, and Pb 5d, respectively. Consequently, the HCMUE-2 material effectively loaded the Pb^{2+} ions onto its framework. Continuously, the O 1s curve of Pb⊂HCMUE-2 is deconvoluted into four peaks that appeared at 532.1, 531.1, 529.9, and 529.3 eV, which are attributed to the Zr–O–H, C–O, Pb–O, and Zr–O–Zr bonds, respectively (Fig. 10c). Herein, almost these signals are shifted to the higher binding energy regions compared with the pristine HCMUE-2 (531.7 eV for Zr–O–H, 530.9 eV for C–O, and 529.1 eV for Zr–O–Zr) (Fig. 10b).[40,61] Besides, the Pb–O signal is not found in the O 1s spectrum of HCMUE-2. This can be explained by the effective attraction of the Pb^{2+} species and the active uptake sites inside MOFs. Noteworthily, the Pb 4f high-resolution spectrum in the Pb⊂HCMUE-2 sample is divided two peaks at 142.6 and 137.8 eV featuring for Pb $4f_{5/2}$ and Pb $4f_{7/2}$ signals, respectively, which are located at different positions compared to those in pure $Pb(NO_3)_2$ solution (144.5 eV for Pb $4f_{5/2}$ and 139.6 eV for Pb $4f_{7/2}$) (Fig. 10d).[61,65] This is caused by the O components derived from the hydroxyl, carboxylate groups, and the μ-OH-containing clusters that can effectively interact with the Pb^{2+} species to form the Pb-O bonds.

4. Conclusion

In this study, a new OH-modified Zr-based MOF, termed HCMUE-2, was prepared by applying a solvothermal method, and its Pb^{2+} uptake property was observed. The achieved results show that the maximum adsorption capacity of Pb^{2+} onto HCMUE-2 reaches a value of 1115.9 mg g^{-1} at pH = 5.5. To the best of our knowledge, this value is one of the greatest Pb^{2+} uptake capacities compared with those of previous studies. Furthermore, the removal of Pb^{2+} is a chemisorption process in high accordance with the Langmuir isotherm and pseudo-second-order kinetic models. Moreover, the reusable investigations indicate that the Pb^{2+} removal level is retained for at least seven cycles without a considerable decrease. In particular, the adsorption mechanism is interpreted *via* a series of combined analytical procedures. All obtained evidence reveals that the uptake mechanism can be proposed by the generation of robust chemical bonds through the electrostatic attraction and electron sharing of oxygen atoms in the hydroxyl moieties present in the MOF structure and the Pb^{2+} ions. Additionally, theoretical calculations should be performed in subsequent studies to clarify further adsorption mechanisms. These discoveries prove that HCMUE-2 is a promising candidate as an efficient adsorbent in eliminating Pb^{2+} from an aqueous medium.

Author contributions

M. V. N formulated this project. M. V. N., H. M. N. P., A. V. N. P., A. N. T. P., V. P. N., H. N. N., T. M. N. synthesized the linker, MOF material and collected PXRD patterns, FT-IR and Raman spectra, TGA-DSC, SEM-EDX-mapping, TEM, and XPS analyses. M. V. N. wrote the paper, and all authors contributed to revising it. All authors have given approval to the final version of the manuscript.

Conflicts of interest

The authors maintain that they have no conflict of interest for this communication.

Acknowledgements

This work was supported by Ho Chi Minh City University of Education, Ho Chi Minh City, Vietnam, through Grant No. CS.2023.19.37.

Notes and references

1 N. A. A. Qasem, R. H. Mohammed and D. U. Lawal, Removal of heavy metal ions from wastewater: a comprehensive and critical review, *npj Clean Water*, 2021, **4**, 36.
2 H. N. M. E. Mahmud, A. K. O. Huq and R. B. Yahya, The removal of heavy metal ions from wastewater/aqueous solution using polypyrrole-based adsorbents: a review, *RSC Adv.*, 2016, **6**, 14778–14791.
3 M. E. Mahmoud, M. M. Osman, A. A. Yakout and A. M. Abdelfattah, Water and soil decontamination of toxic heavy metals using aminosilica-functionalized-ionic liquid nanocomposite, *J. Mol. Liq.*, 2018, **266**, 834–845.
4 P. Shao, D. Liang, L. Yang, H. Shi, Z. Xiong, L. Ding, X. Yin, K. Zhang and X. Luo, Evaluating the adsorptivity of organo-functionalized silica nanoparticles towards heavy metals: quantitative comparison and mechanistic insight, *J. Hazard. Mater.*, 2020, **387**, 121676.
5 H. Shirzadi and A. Nezamzadeh-Ejhieh, An efficient modified zeolite for simultaneous removal of Pb(II) and Hg(II) from aqueous solution, *J. Mol. Liq.*, 2017, **230**, 221–229.
6 M. A. P. Cechinel, S. M. A. G. U. D. Souza and A. A. U. D. Souza, Study of lead (II) adsorption onto activated carbon originating from cow bone, *J. Cleaner Prod.*, 2014, **65**, 342–349.
7 D. Kavak, Removal of lead from aqueous solutions by precipitation: statistical analysis and modeling, *Desalin. Water Treat.*, 2013, **51**, 1720–1726.
8 L. Largitte, S. Gervelas, T. Tant, P. Couespel Dumesnil, A. Hightower, R. Yasami, Y. Bercion and P. Lodewyckx, Removal of lead from aqueous solutions by adsorption with surface precipitation, *Adsorption*, 2014, **20**, 689–700.
9 Q. Dong, X. Guo, X. Huang, L. Liu, R. Tallon, B. Taylor and J. Chen, Selective removal of lead ions through capacitive deionization: Role of ion-exchange membrane, *Chem. Eng. J.*, 2021, **369**, 1535–1542.

10 J. Qian, Z. Zeng, W. Xue and Q. Guo, Lead removal from aqueous solutions by 732 cation-exchange resin, *Can. J. Chem. Eng.*, 2015, **94**, 142–150.
11 W. Xu, X. Sun, M. Huang, X. Pan, X. Huang and H. Zhuang, Novel covalent organic framework/PVDF ultrafiltration membranes with antifouling and lead removal performance, *J. Environ. Manage.*, 2020, **269**, 110758.
12 D. K. Jana, K. Roy and S. Dey, Comparative assessment on lead removal using micellar-enhanced ultrafiltration (MEUF) based on a type-2 fuzzy logic and response surface methodology, *Sep. Purif. Technol.*, 2018, **207**, 28–41.
13 H. Saleem, U. Rafique and R. P. Davies, Investigations on post-synthetically modified UiO-66-NH_2 for the adsorptive removal of heavy metal ions from aqueous solution, *Microporous Mesoporous Mater.*, 2015, **221**, 238–244.
14 S. Jamshidifard, S. Koushkbaghi, S. Hosseini, S. Rezaei, A. Karamipour, A. Jafari Rad and M. Irani, Incorporation of UiO-66-NH_2 MOF into the PAN/chitosan nanofibers for adsorption and membrane filtration of Pb(II), Cd(II) and Cr(VI) ions from aqueous solutions, *J. Hazard. Mater.*, 2019, **368**, 10–20.
15 L. Huang, M. He, B. Chen and B. Hu, Magnetic Zr-MOFs nanocomposites for rapid removal of heavy metal ions and dyes from water, *Chemosphere*, 2018, **199**, 435–444.
16 Q. Zhang, S. Bilisetty, Y. Cao, S. Handschin, J. Adamcik, Q. Peng and R. Mezzenga, Selective and efficient removal of fluoride from water by in situ engineered amyloid fibrils-ZrO_2 hybrid membranes, *Angew. Chem., Int. Ed.*, 2019, **58**, 6012–6016.
17 A. E. Burakov, E. V. Galunin, I. V. Burakova, A. E. Kucherova, S. Agarwal, A. G. Tkachev and V. K. Gupta, Adsorption of heavy metals on conventional and nanostructured materials for wastewater treatment purposes: A review, *Ecotoxicol. Environ. Saf.*, 2018, **148**, 702–712.
18 L. Ma, Q. Wang, S. M. Islam, Y. Liu, S. Ma and M. G. Kanatzidis, Highly selective and efficient removal of heavy metals by layered double hydroxide intercalated with the MoS_4^{2-} ion, *J. Am. Chem. Soc.*, 2016, **138**, 2858–2866.
19 L. Tang, S. Gou, Y. He, L. Liu, S. Fang, W. Duan and T. Liu, An efficient chitosan-based adsorption material containing phosphoric acid and amidoxime groups for the enrichment of Cu(II) and Ni(II) from water, *J. Mol. Liq.*, 2021, **331**, 115815.
20 T.-D. Nguyen-Phan, V. H. Pham, E. W. Shin, H.-D. Pham, S. Kim, J. S. Chung, E. J. Kim and S. H. Hur, The role of graphene oxide content on the adsorption-enhanced photocatalysis of titanium dioxide/graphene oxide composites, *Chem. Eng. J.*, 2011, **170**, 226–232.
21 X. Lu, F. Wang, X. Y. Li, K. Shih and E. Y. Zeng, Adsorption and thermal stabilization of Pb^{2+} and Cu^{2+} by zeolite, *Ind. Eng. Chem. Res.*, 2016, **55**, 8767–8773.
22 D. Kołodyńska, J. Krukowska and P. Thomas, Comparison of sorption and desorption studies of heavy metal ions from biochar and commercial active carbon, *Chem. Eng. J.*, 2017, **307**, 353–363.
23 H. Furukawa, K. E. Cordova, M. O'Keeffe and O. M. Yaghi, The chemistry and applications of metal-organic frameworks, *Science*, 2013, **341**, 1230444.
24 Y. Li, C. Wang, X. Zeng, X. Sun, C. Zhao, H. Fu and P. Wang, Seignette salt induced defects in Zr-MOFs for boosted Pb(II) adsorption: universal strategy and mechanism insight, *Chem. Eng. J.*, 2022, **442**, 136276.
25 D. T. Nguyen, H. N. Nguyen, T. M. Nguyen, H. C. Dong, N. N. Dang, Q.-H. Tran, T. A. Nguyen, M. V. Tran, T. L. H. Doan, L. C. Luu and M. V. Nguyen, An excellent photodegradation efficiency of methylene blue and rhodamine B dyes in a series of porphyrinic Aluminum-based MOFs metallated by copper and cobalt metals, *Colloids Surf., A*, 2024, **689**, 133663.
26 M. V. Nguyen, H. C. Dong, V. T. N. Truong, H. N. Nguyen, L. C. Luu, N. N. Dang and T. A. T. Nguyen, A new porphyrinic vanadium-based MOF constructed from infinite $V(OH)O_4$ chains: syntheses, characterization and photoabsorption properties, *New J. Chem.*, 2022, **46**, 632–641.
27 Q. Shang, N. Liu, D. You, Q. Chen, G. Liao and Z. Pan, The application of Ni and Cu-MOFs as highly efficient catalysts for visible light-driven tetracycline degradation and hydrogen production, *J. Mater. Chem. C*, 2021, **9**, 238–248.
28 K. Manna, R. Kumar, A. Sundaresan and S. Natarajan, Fixing CO_2 under Atmospheric Conditions and Dual Functional Heterogeneous Catalysis Employing Cu MOFs: Polymorphism, Single-Crystal-to-Single-Crystal (SCSC) Transformation and Magnetic Studies, *Inorg. Chem.*, 2023, **62**, 13738–13756.
29 H. Daglar and S. Keskin, Recent advances, opportunities, and challenges in high-throughput computational screening of MOFs for gas separations, *Coord. Chem. Rev.*, 2020, **422**, 213470.
30 W. Sun, J. Hu, S. Duttwyler, L. Wang, R. Krishna and Y. Zhang, Highly selective gas separation by two isostructural boron cluster pillared MOFs, *Sep. Purif. Technol.*, 2022, **283**, 120220.
31 C. Fan, X. Zhang, N. Li, C. Xu, R. Wu, B. Zhu, G. Zhang, S. Bi and Y. Fan, Zn-MOFs based luminescent sensors for selective and highly sensitive detection of Fe^{3+} and tetracycline antibiotic, *J. Pharm. Biomed. Anal.*, 2020, **188**, 113444.
32 A. Liang, S. Tang, M. Liu, Y. Yi, B. Xie, H. Hou and A. Luo, A molecularly imprinted electrochemical sensor with tunable electrosynthesized Cu-MOFs modification for ultrasensitive detection of human IgG, *Bioelectrochemistry*, 2022, **146**, 108154.
33 Y. Chen, Y. Zhang, Q. Huang, X. Lin, A. Zeb, Y. Wu, Z. Xu and X. Xu, Recent advances in Cu-based metal-organic frameworks and their derivatives for battery applications, *ACS Appl. Energy Mater.*, 2022, **5**, 7842–7873.
34 M. V. Nguyen, T. B. Phan, M. V. Tran, T. A. T. Nguyen and H. N. Nguyen, A confinement of N-heterocyclic molecules in a metal-organic framework for enhancing significant proton conductivity, *RSC Adv.*, 2022, **12**, 355–364.
35 J. Zhong, J. Zhou, M. Xiao, J. Liu, J. Shen, J. Liu and S. Ren, Design and syntheses of functionalized copper-based MOFs and its adsorption behavior for Pb(II), *Chin. Chem. Lett.*, 2022, **33**, 973–978.
36 S. Miao, J. Guo, Z. Deng, J. Yu and Y. Dai, Adsorption and reduction of Cr(VI) in water by iron-based metal-organic

frameworks (Fe-MOFs) composite electrospun nanofibrous membranes, *J. Cleaner Prod.*, 2022, **370**, 133566.

37 T. T. M. Bui, L. T. Nguyen, N. P. H. Pham, C. C. Tran, L. T. Nguyen, T. A. Nguyen, H. N. Nguyen and M. V. Nguyen, A new approach for ultra-high adsorption of cationic methylene blue in a Zr-sulfonic-based metal-organic framework, *RSC Adv.*, 2021, **11**, 36626–36635.

38 K. M. V. Nguyen, A. V. N. Phan, N. T. Dang, T. Q. Tran, H. K. Duong, H. N. Nguyen and M. V. Nguyen, Efficiently improving the adsorption capacity of the Rhodamine B dye in a SO_3H-functionalized chromium-based metal-organic framework, *Mater. Adv.*, 2023, **4**, 2636–2647.

39 N. Yin, K. Wang and Z. Li, Rapid microwave-promoted synthesis of Zr-MOFs: an efficient adsorbent for Pb(II) removal, *Chem. Lett.*, 2016, **45**, 625–627.

40 C. C. Tran, H. C. Dong, V. T. N. Truong, T. T. M. Bui, H. N. Nguyen, T. A. T. Nguyen, N. N. Dang and M. V. Nguyen, Enhancing the remarkable adsorption of Pb^{2+} in a series of sulfonic-functionalized Zr-based MOFs: a combined theoretical and experimental study for elucidating the adsorption mechanism, *Dalton Trans.*, 2022, **51**, 7503–7516.

41 W. Zhao, L. Li, J. Liao, R. Liang, A. Song, F. Zhang, H. Ke and J. Qiu, Regenerable and stable biomimetic hydroxyl-modified metal-organic frameworks for targeted uranium capture, *Chem. Eng. J.*, 2022, **433**, 133787.

42 L. Zhai, X. Zheng, M. Liu, X. Wang, W. Li, X. Zhu, A. Yuan, Y. Xu and P. Song, Tuning surface functionalizations of UiO-66 towards high adsorption capacity and selectivity eliminations for heavy metal ions, *Inorg. Chem. Commun.*, 2023, **154**, 110937.

43 Y. Yu, D. Jiang, B. He, B. Yo, X. Pu, D. Liu, W. Xiong, N. Liu and G. Yuan, Facile preparation of UiO-66 derivatives for the removal of Co(II) from aqueous solution: study on adsorption properties and irradiation stability, *J. Radioanal. Nucl. Chem.*, 2023, **332**, 4047–4056.

44 I. Spanopoulos, P. Xydias, C. D. Malliakas and P. N. Trikalitis, A straight forward route for the development of metal-organic frameworks functionalized with aromatic −OH groups: synthesis, characterization, and gas (N_2, Ar, H_2, CO_2, CH_4, NH_3) sorption properties, *Inorg. Chem.*, 2013, **52**, 855–862.

45 S. Bhowal and A. Ghosh, Highly selective fluorescent turn-on-off sensing of OH−, Al^{3+} and Fe^{3+} ions by tuning ESIPT in metal organic frameworks and mitochondria targeted bio-imaging, *RSC Adv.*, 2021, **11**, 27787–27800.

46 H. Zhu, J. Yuan, X. Tan, W. Zhang, M. Fang and X. Wang, Efficient removal of Pb^{2+} by Tb-MOFs: identifying the adsorption mechanism through experimental and theoretical investigations, *Environ. Sci.: Nano*, 2019, **6**, 261–272.

47 Z. Niu, S. Zhang, M. Ma, Z. Wang, H. Zhao and Y. Wang, Synthesis of novel waste batteries-sawdust-based adsorbent *via* a two-stage activation method for Pb^{2+} removal, *Environ. Sci. Pollut. Res.*, 2019, **26**, 4730–4745.

48 X. Yang, S. Yang, S. Yang, J. Hu, X. Tan and X. Wang, Effect of pH, ionic strength and temperature on sorption of Pb(II) on NKF-6 zeolite studied by batch technique, *Chem. Eng. J.*, 2011, **168**, 86–93.

49 H. Kim, D. Kim, D. Moon, Y. N. Choi, S. B. Baek and M. S. Lah, Symmetry-guided syntheses of mixed-linker Zr metal-organic frameworks with precise linker locations, *Chem. Sci.*, 2019, **10**, 5801–5806.

50 X. Wang and Y. Li, Nanoporous carbons derived from MOFs as metal-free catalysts for selective aerobic oxidations, *J. Mater. Chem. A*, 2016, **4**, 5247–5257.

51 X. Luo, L. Ding and J. Luo, Adsorptive removal of Pb(II) ions from aqueous samples with amino-functionalization of metal-organic frameworks MIL-101-Cr, *J. Chem. Eng. Data*, 2015, **60**, 1732–1743.

52 X. Zhu, J. Gu, Y. Wang, B. Li, Y. Li, W. Zhao and J. Shi, Inherent anchorages in UiO-66 nanoparticles for efficient capture of alendronate and its mediated release, *Chem. Commun.*, 2014, **50**, 8779–8782.

53 M. Hinoa and K. Aratab, Synthesis of solid superacid of tungsten oxide supported on zirconia and its catalytic action for reactions of butane and pentane, *J. Chem. Soc., Chem. Commun.*, 1988, 1259–1260.

54 C. Ma, H. T. Wolterbeek, A. G. Denkova and P. S. Crespo, Porphyrinic metal-organic frameworks as molybdenum adsorbents for the $^{99}Mo/^{99m}Tc$ generator, *Inorg. Chem. Front.*, 2023, **10**, 2239–2249.

55 M. Naushad, T. Ahamad, B. M. Al-Maswari, A. Abdullah Alqadami and S. M. Alshehri, Nickel ferrite bearing nitrogen-doped mesoporous carbon as efficient adsorbent for the removal of highly toxic metal ion from aqueous medium, *Chem. Eng. J.*, 2017, **330**, 1351–1360.

56 J. Acharyaa, J. N. Sahu, C. R. Mohanty and B. C. Meikap, Removal of lead(II) from wastewater by activated carbon developed from Tamarind wood by zinc chloride activation, *Chem. Eng. J.*, 2009, **149**, 249–262.

57 H. Zhu, X. Tan, L. Tan, C. Chen, N. S. Alharbi, T. Hayat, M. Fang and X. Wang, Biochar derived from sawdust embedded with molybdenum disulfide for highly selective removal of Pb^{2+}, *ACS Appl. Nano Mater.*, 2018, **1**, 2689–2698.

58 X. Wang, S. Xia, L. Chen, J. Zhao, J. Chovelon and J. Nicole, Biosorption of cadmium(II) and lead(II) ions from aqueous solutions onto dried activated sludge, *J. Environ. Sci.*, 2006, **28**, 840–844.

59 M. Lu, L. Li, S. Shen, D. Chen and W. Han, Highly efficient removal of Pb^{2+} by a sandwich structure of metal–organic framework/GO composite with enhanced stability, *New J. Chem.*, 2019, **43**, 1032–1037.

60 X. Luo, L. Ding and J. Luo, Adsorptive removal of Pb(II) ions from aqueous samples with amino-functionalization of metal-organic frameworks MIL-101(Cr), *J. Chem. Eng. Data*, 2015, **60**, 1732–1743.

61 X. Zhao, Y. Wang, Y. Li, W. Xue, J. Li, H. Wu, Y. Zhang, B. Li, W. Liu, Z. Gao and H. Huang, Synergy effect of pore structure and amount of carboxyl site for effective removal of Pb^{2+} in metal-organic frameworks, *J. Chem. Eng. Data*, 2019, **64**, 2728–2735.

62 E. Tahmasebi, M. Y. Masoomi, Y. Yamini and A. Morsali, Application of mechanosynthesized azine-decorated Zinc(II) metal-organic frameworks for highly efficient removal and

extraction of some heavy-metal ions from aqueous samples: a comparative study, *Inorg. Chem.*, 2015, **54**, 425–433.

63 C.-X. Yu, K.-Z. Wang, X.-J. Li, D. Liu, L.-F. Ma and L.-L. Liu, Highly efficient and facile removal of Pb^{2+} from water by using a negatively charged azoxy-functionalized metal–organic framework, *Cryst. Growth Des.*, 2020, **20**, 5251–5260.

64 A. Hakimifar and A. Morsali, Urea-based metal–organic frameworks as high and fast adsorbent for Hg^{2+} and Pb^{2+} removal from water, *Inorg. Chem.*, 2019, **58**, 180–187.

65 C. X. Yu, K. Z. Wang, X. J. Li, D. Liu, L. F. Ma and L. L. Liu, Highly efficient and facile removal of Pb^{2+} from water by using a negatively charged azoxy-functionalized metal-organic framework, *Cryst. Growth Des.*, 2020, **20**, 5251–5260.